Accepted for publication in *The Astrophysical Journal*

# The First Reported Infrared Emission from the SN 1006 Remnant

P. Frank Winkler[1], Brian J. Williams[2], William P. Blair[3] Kazimierz J. Borkowski[4], Parviz Ghavamian[5], Knox S. Long[6], John C. Raymond[7], and Stephen P. Reynolds[4]

## ABSTRACT

We report results of infrared imaging and spectroscopic observations of the SN 1006 remnant, carried out with the *Spitzer* Space Telescope. The 24 $\mu$m image from MIPS clearly shows faint filamentary emission along the northwest rim of the remnant shell, nearly coincident with the Balmer filaments that delineate the present position of the expanding shock. The 24 $\mu$m emission traces the Balmer filaments almost perfectly, but lies a few arcsec within, indicating an origin in interstellar dust heated by the shock. Subsequent decline in the IR behind the shock is presumably due largely to grain destruction through sputtering. The emission drops far more rapidly than current models predict, however, even for a higher proportion of small grains than would be found closer to the Galactic plane. The rapid drop may result in part from a grain density that has always been lower—a relic effect from an earlier epoch when the shock was encountering a lower density—but higher grain destruction rates still seem to be required. Spectra from three positions along the NW filament from the IRS instrument all show only a featureless continuum, consistent with thermal emission from

[1]Department of Physics, Middlebury College, Middlebury, VT 05753; winkler@middlebury.edu

[2]NASA Goddard Space Flight Center, Greenbelt, MD 20771; brian.j.williams@nasa.gov

[3]Department of Physics and Astronomy, Johns Hopkins University, 3400 N. Charles St., Baltimore, MD 21218; wpb@pha.jhu.edu

[4]Physics Department, North Carolina State University, Raleigh, NC 27695; kborkow@ncsu.edu, reynolds@ncsu.edu

[5]Department of Physics, Astronomy and Geosciences, Towson University, Towson, MD, 21252; pghavamian@towson.edu

[6]Space Telescope Science Institute, 3700 San Martin Drive, Baltimore MD 21218; long@stsci.edu

[7]Harvard-Smithsonian Center for Astrophysics, 60 Garden Street, Cambridge, MA 02138; jraymond@cfa.harvard.edu

warm dust. The dust-to-gas mass ratio in the pre-shock interstellar medium is lower than that expected for the Galactic ISM—as has also been observed in the analysis of IR emission from other SNRs but whose cause remains unclear. As with other SN Ia remnants, SN 1006 shows no evidence for dust grain formation in the supernova ejecta.

*Subject headings:* ISM: individual (SNR SN1006) — ISM: kinematics and dynamics — shock waves — supernova remnants

## 1. Introduction

The supernova of 1006 C.E. is generally recognized as the brightest stellar event in recorded human history, with surviving contemporary reports from China, Japan, Korea, the Arab world, and in Europe as far north as St. Gallen, Switzerland (latitude 47.4° N), all despite the supernova's southern declination of Decl. (1006) = −38.5° (Stephenson 2010). Throughout much of the twentieth century, SN 1006 languished in relative obscurity compared with the attention lavished on the other eleventh-century supernova, SN 1054, that gave rise to the Crab Nebula. But once Goldstein (1965) called attention to the event and Marsden (1965) constrained its location, radio emission from the SN 1006 remnant was soon discovered by Gardner & Milne (1965). It has since become a widely observed and important object: X-rays from SN 1006 were discovered by Winkler & Laird (1976); optical emission by van den Bergh (1976); and (following a somewhat checkered history) TeV $\gamma$-rays were definitively detected and mapped by the HESS collaboration (Acero et al. 2010). Koyama et al. (1995) discovered that the NE and SW limbs of SN 1006 have a featureless, power-law X-ray spectrum, providing the first conclusive evidence that electrons can be accelerated to TeV energies in supernova shocks and cementing the long-suspected connection between supernovae and cosmic rays. Yet no infrared emission has previously been reported from SN 1006.

The SN 1006 remnant has a limb-brightened shell, 30′ in diameter with strong bi-lateral symmetry in radio and X-rays. Its distance is well determined at 2.2 kpc (Winkler et al. 2003), and it is located high above the Galactic plane ($b_{\rm II} = 14.6°$, $z = 550$ pc). Its high-latitude location leads to relatively low foreground absorption. SN 1006 itself was almost certainly a Type Ia event, based on its location, environment far from any recent star formation, apparent absence of any compact remnant, and implication from Chinese records that it remained visible for several years (Stephenson & Clark 2002). The optical emission from its remnant consists solely of Balmer-dominated filaments (e.g., Schweizer & Lasker 1978; Kirshner et al. 1987; Ghavamian et al. 2002), which indicate that it is expanding into an environment with relatively low density that is at least partially neutral, another signature

of SN Ia remnants.

Supernovae and their remnants are critical to dust grain formation, modification, and destruction. Dust grains may condense from metal-rich SN ejecta, and the fast shock waves in SNRs can lead to sputtering through collisions with shock-heated gas that erode and eventually destroy dust grains (e.g., Dwek & Scalo 1980; Draine 2003; Sankrit et al. 2010). Although these processes have been observed in a number of SNRs, SN 1006 nevertheless provides a unique perspective due to its location high above the Galactic plane in a relatively pristine region of the ISM. There is growing observational evidence for the formation of dust in the ejecta from core-collapse SNe, including SN 1987A (Wooden et al. 1993; de Kool et al. 1998; Matsuura et al. 2011), Cas A (Rho et al. 2008; Nozawa et al. 2010), and the Crab Nebula (Gomez et al. 2012b), and in the late-time emission from a number of more distant SNe, (e.g., Kotak et al. 2009; Szalai et al. 2011; Meikle et al. 2011).

Recent models by Nozawa et al. (2011) predict that small dust grains can also form in the ejecta from Type Ia SNe, and that $10^{-3} M_{\odot}$ of dust can survive for $\sim 1000$ years. However, no dust associated with ejecta has as yet been observed in any of historical remnants of the SN Ia: Tycho (SN 1572), Kepler SN 1604), or RCW86 (probable SN 185 remnant), all of which have been widely observed in the infrared. Mid-IR emission from both Tycho and Kepler was detected from the InfraRed Astronomy Satellite (IRAS, Braun 1987), and both have been observed in detail from ISO (Douvion et al. 2001), *Spitzer* (Blair et al. 2007; Williams et al. 2012), *Herschel* (Gomez et al. 2012a), and other missions. RCW86 was also detected from IRAS (Arendt 1989; Saken et al. 1992), and Williams et al. (2011a) have recently presented detailed observations with *Spitzer*. Borkowski et al. (2006) have also reported IR observations for four SN Ia remnants in the Large Magellanic Cloud. All these cases show thermal emission from dust grains and provide evidence for grain destruction in SN shocks, but none shows convincing evidence for grain *formation* (see especially Gomez et al. 2012a).

In this paper we report the first detection of IR emission from the SN 1006 remnant. In Sections 2 and 3 we describe the results of an imaging mapping campaign with the *Spitzer* Space Telescope, which reveals a filament of $24\,\mu$m emission along the NW limb of the shell, plus very faint, diffuse emission elsewhere. In Section 4 we describe the spectroscopic observations from the InfraRed Spectrometer (IRS) on *Spitzer*, and in Section 5 we present a discussion in which we fit dust models to both sets of data and assess the total dust mass and dust-to-gas mass ratio. Finally, we give a brief summary of our results in Section 6.

## 2. MIPS Observations

We mapped SN 1006 twice with the Multiband Imaging Photometer for *Spitzer* (MIPS, Rieke et al. 2004) as part of program 30673: on 2007 March 5 and 2007 August 22. In order to cover the entire 30′ shell and the surrounding background field, each observation required a pair of overlapping scan maps, which were taken consecutively. The March AORs (18724608 and 18725120) were carried out during a "cold" campaign and included observations at 24$\mu$m, 70$\mu$m, and 160$\mu$m, while the August ones (18724864 and 18725376) were during a "warm" phase of the cryogenic mission and gave only 24$\mu$m and 70$\mu$m data. Both pairs of scans consisted of 14 legs of length 0.75°; offsets of 148″ were used for the March pair, while the August pair used offsets of 111″ to give greater exposure of SN 1006 itself at a cost of somewhat less surrounding background. We began with Basic Calibrated Data (BCD) files from the *Spitzer* Heritage Archive that had been processed through version 18.12 of the *Spitzer* pipeline, and we then performed further flat-fielding by taking a median of the hundreds of frames from each AOR, and dividing all the frames from that AOR by the normalized flat. The estimated zodiacal light was then subtracted from each frame, and the maps were mosaicked together onto a standard world coordinate system, 50′ square with 1″ pixels, using the MOPEX software provided by the *Spitzer* Science Center. Finally, we used DAOPHOT in IRAF[1] to remove the vast majority of point sources (mainly stars) from the mosaic image, in order to better assess the diffuse emission from SN 1006 itself.

The full 24 $\mu$m mosaic is shown in Fig. 1, with both the original and star-subtracted versions in panels *a* and *b*, respectively. These clearly show the first detection of SN 1006 in the mid-infrared. For reference, we also show images of the identical SN 1006 field in H$\alpha$, X-rays, and radio in other panels of the figure. The most prominent IR feature is the thin filament along the NW rim of the shell. Even this brightest emission is quite faint, with peak surface brightness levels above the background of 0.25 - 0.3 MJy sr$^{-1}$, only about 6% of the background emission and fainter than either the Tycho or Kepler SNRs by more than a factor of 20. The integrated flux from this filament in the 24$\mu$m band is $F(24\mu\mathrm{m}) = 130 \pm 30$ mJy, where the precision is limited by our tracing of the filament and ability to assess the background accurately, since there is diffuse background as well as faint residual stars in the "star-subtracted" mosaic.

We used a similar approach for the 70 $\mu$m data, except that here the mosaic has a scale of 4″ pixel$^{-1}$. Despite our flat-fielding all the data using median frames for each AOR,

[1]IRAF is distributed by the National Optical Astronomy Observatory, which is operated by the Association of Universities for Research in Astronomy, Inc., under cooperative agreement with the National Science Foundation.

artifacts along the scan directions are nevertheless evident in the final mosaic, shown in the bottom left panel of Fig. 1. There is the slightest hint of an enhancement in the region of the NW filament, but this does not trace the narrow filament and is barely larger than background fluctuations in the vicinity. We give only an upper limit for the average surface brightness in the region of the filament: $S(70\mu\mathrm{m}) < 0.85$ MJy sr$^{-1}$ ($3\sigma$), and an integrated flux $F(70\mu\mathrm{m}) < 800$ mJy. The 160 $\mu$m images, compiled using only the two scans from 2007 March for which 160 $\mu$m are available, are quite noisy and show no discernible emission from SN 1006.

## 3. Imaging Analysis and Multi-wavelength Comparisons

### 3.1. The Northwest Filament

The NW filament corresponds closely with the optical filament that appears only in the hydrogen Balmer lines (van den Bergh 1976; Winkler et al. 2003; Raymond et al. 2007), as shown in the deep continuum-subtracted image shown in the lower right panel of Fig. 1. Such "nonradiative" filaments characterize fast shocks expanding into a low-density, partially neutral environment, and that are generally associated with relatively young remnants from Type Ia supernovae such as SN 1006. Balmer emission from these filaments has two components, both the result of neutral H atoms that cruise through the shock. In the hot post-shock environment, the neutrals can be excited and decay to produce narrow lines (with a width characteristic of the pre-shock temperature), or they can undergo charge exchange with hot protons to produce broad lines whose width is closely related to the post-shock proton temperature (e.g., Chevalier et al. 1980; Ghavamian et al. 2002; Heng 2010). Since the lifetime of neutral atoms in the hot post-shock environment is very short, the Balmer filaments can occur only *immediately* behind the shock, and thus delineate the current position of the shock.

To investigate the post-shock characteristics of emission along the NW filament in various bands, we have compared 24$\mu$m, H$\alpha$, and X-ray images. We have used a higher resolution H$\alpha$ image, taken from the 0.9 m telescope at CTIO on 2002 March 21, for which the stars were subtracted using a matched continuum image (for details, see Winkler et al. 2003), instead of the one shown in Fig. 1c. Likewise, in X-rays we have used the 0.5-2.0 keV data from a 90 ks observation taken 2001 April 26-27 with the *Chandra* ACIS-S (for details, see Long et al. 2003), rather than the mosaic of shorter ACIS-I exposures used in Fig. 1e. We

first checked the alignment of all three images[2] using four near point sources common to all: one bright star and three distant galaxies, and found their positions in all three bands to agree within 0.5″. To simulate images in all three bands at a common epoch, we used the $\mu = 280 \pm 8$ mas yr$^{-1}$ proper motion rate for the NW Balmer filaments, measured relative to the center of curvature at R.A. (2000.) = $15^{\rm h}\,03^{\rm m}\,16\overset{\rm s}{.}2$, Decl. (2000.) = $-42^\circ\,00'\,30''$ by Winkler et al. (2003), to extrapolate the H$\alpha$ and X-ray images from their original epochs (2002.2 and 2001.3, respectively) to the 2007.5 mean epoch for the *Spitzer* MIPS scans. (Recent measurements from *Chandra* find X-ray proper motions along most of the NW rim of SN 1006 that agree with those measured for the optical filaments, Katsuda et al. 2012).

In Fig. 2 we show a three-color combination that compares the 24 $\mu$m (red), H$\alpha$(green), and X-ray (blue) images of the NW filament, and in Fig. 3 we plot radial profiles taken perpendicular to the filament, integrated over the four azimuthal regions outlined in Fig. 2. It is clear that the 24 $\mu$m emission has a broader spatial profile that peaks 3 - 5 arcsec behind the Balmer filament, as best illustrated in region D of Fig. 3 where the profiles are the cleanest. The filament is also noticeably broader in the IR than in H$\alpha$, with FWHM $\gtrsim 15''$. This is not simply a resolution effect. The resolution of the 24 $\mu$m mosaic image—measured from profiles of several isolated stars—is 6″ (FWHM), consistent with the diffraction limit, but small compared with the width of the filament.

We attribute this IR emission to dust from the ISM that enters the shock, where it is heated through collisions with hot post-shock gas, produces IR emission, and is then destroyed. Somewhat further behind the shock, soft, primarily thermal, X-ray emission appears, rising to its peak about 10″ behind the shock, just as the 24 $\mu$m emission is decaying away. This indicates the longer time scale for producing the highly ionized species that radiate efficiently and dominate the X-ray emission (Long et al. 2003). We can estimate the time scales through simple kinematics: the primary shock is moving outward to the NW at $\mu = 280 \pm 8$ mas yr$^{-1}$, and if we assume the nominal compression ratio of 4 between the post-shock and pre-shock densities, the post-shock material is dropping behind the shock at speed $v_s/4$, or $\mu = 70$ mas yr$^{-1}$ (relative to the shock). Therefore, the IR peak occurs some 60 yr after that material was shocked, and the X-ray peak occurs $\sim 150$ yr after the shock. We shall discuss the emission profiles further in Sec. 5.1 of this paper.

In 2012 March, all-sky survey data from the Wide-field Infrared Survey Explorer (WISE, Wright et al. 2010) were released.[3] Examination of data from the SN 1006 region in all the

[2]For checking the H$\alpha$ image we of course used the version *before* continuum subtraction; the coordinates for the subtracted image are identical.

[3] see http://wise2.ipac.caltech.edu/docs/release/allsky/.

WISE bands (3.4, 4.6, 12 and 22 $\mu$m) shows emission from SN 1006 only in the 22 $\mu$m band. Not surprisingly, the WISE 22 $\mu$m image is very similar to the *Spitzer* 24 $\mu$m one, and clearly shows the NW filament. However, the WISE data have somewhat lower angular resolution and signal-to-noise than that from *Spitzer*. The non-detection of emission in the shorter-wavelength *WISE* bands is consistent with the lack of short-wavelength emission in other Type Ia remnants (Borkowski et al. 2006). Close examination of the images from the Improved Reprocessing of the IRAS Survey (IRIS; Miville-Deschênes & Lagache 2005) also shows traces of the NW filament in the co-added 25 $\mu$m image; however, it is unlikely that this faint feature would ever have been independently discovered in these low-resolution (1.5′) maps.

### 3.2. Other Faint IR Emission

In addition to the narrow filaments along the NW rim of the shell, there is patchy, diffuse emission within much of the southern part of the SN 1006 shell, clearly visible in the 24 $\mu$m mosaic and less so in the 70 $\mu$m one. The morphology of this emission is similar at both 24 $\mu$m and 70 $\mu$m, and is also similar to patchy emission extending well outside the SN 1006 shell, especially to the south and east. In the southern portion of SN 1006, there is also faint, diffuse emission in both H$\alpha$ and X-rays (Fig. 1c and e), but unlike along the NW rim, the morphology in the south is only vaguely similar to that seen in the IR. In the absence of further data, we cannot determine whether the faint IR emission is associated with SN 1006 itself or stems from cool foreground dust.

In X-rays, SN 1006 shows knots of emission interior to the shock that are thought to arise largely from SN ejecta, but there are no obvious small-scale IR features that correlate with these X-ray-emitting ejecta knots. Hence we find no evidence for the formation of dust in SN 1006 ejecta. This is somewhat surprising in view of theoretical predictions for dust formation in SN Ia ejecta (Nozawa et al. 2011), but is consistent with observations of other Type Ia SNRs (Borkowski et al. 2006; Williams et al. 2012).

## 4. Spectroscopic Observations

We conducted IRS observations, all in Staring mode for about 90 min each, at three locations along the NW filament. We show the slit positions of these IRS pointings, labeled 1-3, in Fig. 4, overlaid on the MIPS 24 $\mu$m image of the filament. As noted earlier, the filament is quite faint in the IR (its average surface brightness is only about 6% above the

background at 24 $\mu$m), and it was undetected in the SL (5.5-14 $\mu$m) spectrum. However, faint emission is detected in the LL order 2 (14-19.3 $\mu$m) spectrum, where the dust continuum begins around 17 $\mu$m and continues to rise throughout the LL order 1 (19-40 $\mu$m) spectrum. We see no evidence for line emission anywhere in the spectrum, consistent with the non-radiative nature of the blast wave shock at this location (Dwek 1987; Dwek et al. 1996; Williams et al. 2011b).

The data used in our analysis (AOR IDs 28138240 and 24142080) were processed with *Spitzer* calibration pipeline version S18.7.0. Using the IDL CUBISM software (Smith et al. 2007), we assembled the 72 BCD files from positions 1 and 2 along the NW filament into two data cubes, one for LL1 and one for LL2. The IRS spectrum from position 3 is similar, but we have omitted it from our subsequent analysis because it falls on a region where different abundances were required to fit the X-ray spectrum (Long et al. 2003). Hot pixels affect the BCDs (especially beyond 35 $\mu$m), so we median smoothed the BCDs before creating the data cubes using the FILTER_IMAGE routine from the IDL Astronomy User's library. The smoothing replaces the value of each pixel with the median of the surrounding 3 pixels in a moving box and significantly mitigates the hot pixels in the resulting data cubes. While the smoothing reduces the spatial resolution of the data somewhat, the emission from the filament is highly uniform and we expect minimal loss of information.

After combining the BCDs within CUBISM, we extracted LL1 and LL2 spectra from the NW filament using positions 1 and 2 marked in Fig 4. These two positions are only $\sim 30''$ apart and their IRS spectra appear virtually identical; therefore, we have combined them into a single object spectrum. To estimate the sky background, we extracted separate LL1 and LL2 spectra from locations just outside SN 1006 (marked in Fig 4). We averaged the two sky spectra in each order and combined them to produce a final sky spectrum. We subtracted this spectrum from that of the SN 1006 filament to obtain the final spectrum shown in Fig. 5. We describe the fits to this spectrum in the following section.

## 5. Discussion

### 5.1. Model Fits to the Data

Infrared emission in typical SNR shocks is produced entirely by collisional heating of dust grains (Dwek & Arendt 1992), where energetic electrons and ions collide with the grains, heating them to temperatures of 50-100 K. Collisions with protons and heavier ions are also responsible for grain sputtering, reducing the size of large grains and destroying many small grains entirely. We have developed models for such dust that self-consistently calculate both

the heating and the destruction of grains in the post-shock gas as a function of the density of the hot plasma, $n_p$, the electron and ion temperatures, and the shock sputtering age $\tau = \int_0^t n_p dt$ (Borkowski et al. 2006). For an arbitrary input grain size distribution, we can use these models to calculate the IR spectrum and the post-shock profile that results as grains are heated, and eventually destroyed.

The electron temperature, $T_e$, and the ionization timescale can be determined from a non-equilibrium ionization analysis of the X-ray spectra, as Long et al. (2003) did for the NW limb using *Chandra* data. We have revisited that analysis, taking into account hydrocarbon contamination of the ACIS detectors that was unrecognized at the time of the original analysis, and using more reliable atomic data. We first redetermined the absorption column density $N_{\rm H}$ from the reprocessed synchrotron-dominated eastern limb data (region NE-1 of Long et al. 2003), fit using XSPEC (Arnaud 1996) with a pure synchrotron *srcut* model to obtain $N_{\rm H} = (8.2 \pm 0.8) \times 10^{20}$ cm$^{-2}$. We fixed $N_{\rm H}$ at this value in fitting Long et al's region NW-1, which includes our IRS regions 1 and 2. We obtained reasonable fits using a solar-abundance plane-shock model (*vnpshock*), and obtained values of $kT_e = 0.9$ keV, ionization timescale $n_e t = 5.3 \times 10^9\,{\rm cm}^{-3}\,{\rm s} = 170\,{\rm cm}^{-3}\,{\rm yr}$, and emission measure $n_e M_g = 6.2 \times 10^{-3}\ M_\odot$ cm$^{-3}$. This is a somewhat higher electron temperature than the $kT_e = 0.6$ keV found by Long et al. (2003), but is still far below the post-shock proton temperature of $kT_p = 16$ keV, inferred from the Balmer line profiles by Ghavamian et al. (2002). (Vink et al. 2003, also measured a similar value for $T_e$ at a different position along the NW rim.). We then applied a Coulomb-heating model for collisions between electrons and protons behind the shock, and found that over the relatively small region we consider here, the mean proton and electron temperatures are 16 keV and 1.0 keV, respectively. We use these temperatures for the remainder of this work.

Our models also require as input a distribution of grain sizes in the ISM ahead of the shock. A commonly used distribution for the Galaxy is that of Weingartner & Draine (2001). Their models are appropriate for the diffuse ISM in the disk of the Galaxy, where the total-to-selective extinction ratio $R_V \equiv A_V/E(B-V) = 3.1$, and for dense clouds where $R_V > 3.1$. At the location of SN 1006 some 500 pc above the Galactic plane, however, the abundance of dust—both in total amount and in the distribution of grain sizes—is likely very different from that near the Galactic plane. There is significant evidence for much lower values for $R_V$ at high Galactic latitudes (Larson & Whittet 2005). Mazzei & Barbaro (2011) have calculated grain size distributions using the same formalism as Weingartner & Draine (2001) for over 70 lines of sight to stars with "anomalous extinction sightlines." Particularly relevant for our work, they extend these models down to low-density environments with $R_V = 2.0$. We use the model from Table 3 of Mazzei & Barbaro (2011), with $R_V = 2.0$ and $10^5 b_c = 5.0$ (this is a parameterization in their models that corresponds to the number

of small carbonaceous grains). The grain size distributions corresponding to lower values of $R_V$ are steeper than their "typical" Milky Way counterparts, i.e., they have an excess of small grains relative to large ones, resulting in a larger fraction of the total mass in grains being destroyed via sputtering for a given shock, as well as a different gas density required to produce the observed spectrum.

In our models, the spectrum from warm dust is most sensitive to the gas density in post-shock plasma, so we have used proton density $n_p$ as the principal free parameter. Using the grain size distribution described above, we have fit the IRS spectrum over the range 21 - 37 $\mu$m and obtain a best fit for a density of $n_p = 1.4 \pm 0.5\,\mathrm{cm}^{-3}$, shown in blue in Fig. 5. The 21 - 37 $\mu$m range comprises all the data for which the signal-to-noise ratio is high enough to be useful. The uncertainty quoted is a formal 90%-confidence limit based on statistical uncertainties only, determined from the rms deviations from an arbitrary smooth polynomial fit to the spectrum in this range. We have made no provision for systematic errors in the IRS spectra, which are difficult to quantify.

There is good reason to believe that the actual density is near the lower limit of the fitted range, near $n_p = 1\ \mathrm{cm}^{-3}$. From an analysis of the thermal X-ray emission along the NW rim based on *Chandra* observations, Long et al. (2003) found a post-shock electron density $n_e \sim 1\,\mathrm{cm}^{-3}$. Analysis of X-ray data from *XMM-Newton* using a different modeling approach led Acero et al. (2007) to a *pre*-shock density value of $n_0 \sim 0.15\,\mathrm{cm}^{-3}$, equivalent to a post-shock density of $n_p \sim 0.6\,\mathrm{cm}^{-3}$ for a standard compression ration of 4. And finally, an estimate based on the thickness of the H$\alpha$ filaments in an image from the *Hubble* Space Telescope by Raymond et al. (2007), and subsequently corrected by Heng et al. (2007), gave $n_0 = 0.15 - 0.3$, and thus a post-shock density $n_p \sim 1\,\mathrm{cm}^{-3}$. In Fig. 5 we also show, in red, a model with $n_p = 1.0\,\mathrm{cm}^{-3}$, which gives an acceptable fit to the IRS data. Finally, we note that the predicted 70 $\mu$m surface brightness for any of our models is $\lesssim 0.25\,\mathrm{MJy\ sr}^{-1}$, well below the upper limit reported in Section 2.

We have also calculated the spatial profile for the decay of IR emission as grains are destroyed through sputtering in the hot, post-shock environment, assuming that the shock has been advancing through an ambient medium of constant density. In comparing the model with the observed radial profiles, we find that the observed decay is far more rapid than the sputtering model predicts, as illustrated in Fig. 6. Even if we assume a grain-size distribution heavily weighted toward small grains to give $R_V = 2.0$, for a density of $n_\mathrm{H} = 1\,\mathrm{cm}^{-3}$ the sputtering rate would need to be artificially enhanced by a factor 6 to 8 to match the observed profiles.

However, it is almost certain that the shock along the NW rim of SN 1006 has *not* been passing through a uniform-density environment. The ambient density to the NW is clearly

higher than that around the remainder of the shell, as evidenced by the following facts: (1) the flattening of the shell to the NW; (2) the fact that the proper motion along most of the NW limb is only about 60% as high as that to the NE (Katsuda et al. 2012); (3) the density contrast around the shell required from X-ray observations (Long et al. 2003; Acero et al. 2007); and (4) the mere fact that there is significant IR emission along the NW limb, yet little or none elsewhere. Since the shell radius to the NW is only about 15% smaller than elsewhere, the shock must have encountered the denser region there relatively recently. As a result, the post-shock density profile, for both gas and dust, should drop as one moves inward from the shock. Therefore the decrease in IR emission behind the shock is likely due in large part to the fact that farther inward the grain density has always been lower, representing an earlier epoch in the evolution of SN 1006. We suggest that this may account for the rapid drop in IR emission $\sim 20'' - 35''$ behind the shock (Fig. 6). For a density $n_p = 1\,\mathrm{cm}^{-3}$ (equivalent to $n_e = 1.2\,\mathrm{cm}^{-3}$), the shock age from X-ray spectroscopy is about $170/n_e = 140$ years, suggesting that the shock was encountering considerably lower densities earlier. Detailed modeling of such a scenario is beyond the scope of the present paper.

Nevertheless, the fact that the observed post-shock drop in IR emission is so much sharper than predicted by the models, even close to the shock, probably indicates that current models significantly underestimate the actual dust sputtering rate. Effects that could be responsible include an even greater proportion of small grains, grains of high porosity, or a grain composition that leads to higher sputtering rates. Enhanced sputtering rates are not without precedent; Serra Díaz-Cano & Jones (2008) found that hydrogenated dust grains (perhaps the most common type of grains in the ISM, at least for carbonaceous materials) are sputtered at rates several times higher than their pure amorphous counterparts. The spectral data are insufficient to determine whether the carbonaceous grains in SN 1006 are hydrogenated or amorphous.

### 5.2. Dust Mass of the NW Filament

Almost independent of the models, we can determine the total amount of dust radiating in the NW filament, provided that the integrated IR luminosity is relatively well-known. We have used the measured IR flux, $F(24\mu\mathrm{m}) = 130 \pm 30$ mJy (Section 2), and assumed that the overall shape of the dust spectrum observed with IRS (shown in Fig. 5) is applicable along the entire length of the filament to obtain $L_{\mathrm{IR}} = (1.7 \pm 0.9) \times 10^{34}\, d_{2.2}^2$ ergs s$^{-1}$, where we have scaled to a distance of 2.2 kpc: $d_{2.2} \equiv d/2.2$ kpc. Our models assume optical constants from Draine & Lee (1984) for graphite and amorphous silicate grains in the ISM, with relative proportions and grain-size distributions from Mazzei & Barbaro (2011). As

in Williams et al. (2008), we then calculate the dust mass in the NW filament as $M_{\rm dust} = (1.1 \pm 0.6) \times 10^{-5}\, d_{2.2}^2\, M_\odot$, where the uncertainty limits for both $L_{\rm IR}$ and $M_{\rm dust}$ include the overall 15% uncertainty in the *Spitzer* MIPS extended source flux calibration. Of course, this method of determining the total dust mass is insensitive to any cold dust—undetectable with *Spitzer*—but it is difficult to imagine how a significant fraction of interstellar dust (consisting almost entirely of small grains, $a < 0.5\,\mu$m) could remain cold within the hot plasma behind such a fast shock. Our value for $M_{\rm dust}$ includes only the dust now radiating along the NW filament; the overall faintness of the rest of the SNR at $24\,\mu$m, combined with the lack of detection at 70 $\mu$m, precludes determination of a dust mass for the entire remnant.

### 5.3. The Ambient Dust-to-Gas Mass Ratio

In previous works (Borkowski et al. 2006; Sankrit et al. 2010; Williams et al. 2011b,a) we have used the density determination from IR data, combined with the X-ray emission measure, to obtain a measure of the amount of shocked gas present within a given emitting volume. We have obtained the dust mass from the overall normalization to the dust spectrum, so dividing the two gives the dust-to-gas mass ratio. In the case of SN 1006, however, the IRS spectra do not strongly constrain the density. Thus, we employ an alternative approach.

Laming et al. (1996) examined the ultraviolet spectrum of a section of the NW filament obtained with the *Hopkins Ultraviolet Telescope* (*HUT*) and measured 0.02 He II (1640 Å) photons cm$^{-2}$ s$^{-1}$. More recent work by Chayer (private communication) has revised the reddening towards SN 1006 to be $E(B-V) = 0.09$, lowering the He II flux to 0.017 photons cm$^{-2}$ s$^{-1}$. According to the Laming et al. models, 0.0067 He II photons come out for each H atom crossing the shock. For the 200″ section of the filament observed (corresponding to a distance of $6.5 \times 10^{18}$ cm at $d = 2.2$ kpc), the He II flux measured at Earth would be

$$F_{\rm He\,II} = \left(0.0067\ \frac{\rm photons}{\rm H\ atom}\right) \left(6.5 \times 10^{18}\,{\rm cm}\right) \frac{n_0 v_s l}{4\pi d^2}\,,$$

where $n_0$ is the pre-shock H number density, $v_s$ is the shock speed, and $l$ is the line-of-sight depth through the emitting material, all of which are presumed (for this purpose) to be unknown. Taking $F_{\rm He\,II} = 0.017$ photons cm$^{-2}$ s$^{-1}$, we can rearrange the above equation to give $n_0 v_s l = 2.26 \times 10^{26}$ cm$^{-1}$ s$^{-1}$. The length of the NW-1 region is 3′, or $5.9 \times 10^{18}$ cm at $d = 2.2$ kpc, so $1.3 \times 10^{45}$ H atoms per second enter the shock. If we assume a standard post-shock flow of 70 mas yr$^{-1}$, based on the proper motion measurements of Winkler et al. (2003), then the width of the IR filament corresponds to a timescale of 150 years. During this time, the shock will have swept up 6.3 $\times 10^{54}$ H atoms, or 7.6 $\times 10^{-3} M_\odot$ of gas. The

uncertainties in the *HUT* measurement of the He II flux and in the reddening correction are about 15% each, while the uncertainty in proper motion is only 3% and the uncertainty in the relative atomic rates is probably about 30%, so we estimate an uncertainty in the gas mass of $\sim$ 40%. Using the dust mass determined above, this leads to a dust-to-gas mass ratio of $\sim (1.5 \pm 1.0) \times 10^{-3}$. The expected dust-to-gas mass ratio for the Galaxy within the model of Mazzei & Barbaro (2011) is 5.3 $\times 10^{-3}$, a factor of $\sim$ 3 higher than what we measure.

The dust-to-gas mass ratio in the ambient medium surrounding SN 1006 appears to be lower than that expected from dust models for the Galaxy, including those at high Galactic latitudes. This has been the case for virtually all SNRs studied, both in the Galaxy (e.g., Blair et al. 2007; Arendt et al. 2010; Lee et al. 2009) and in the Magellanic Clouds (Borkowski et al. 2006; Williams et al. 2006, 2011b). The ultimate reason for this remains a mystery, but in the case of SN 1006 specifically, its location within the Galaxy may provide a clue. At some 500 pc above the Galactic plane, SN 1006 is located at the interface between the disk and halo (see Putman et al. 2012, for a review of gaseous galaxy halos and their interfaces to galactic disks). Accumulating evidence points to a lower dust content there than in the Galactic disk (Ben Bekhti et al. 2012), coupled with a higher proportion of smaller grains (Planck Collaboration et al. 2011). An expected increase in the sputtering rate for smaller grains might better match the rapid drop-off in the 24 $\mu$m profile behind the shock (Fig. 6) than the current dust model, and it would also raise our inferred value of the pre-shock dust-to-gas mass ratio, bringing it even more in line with the Mazzei & Barbaro (2011) value. We further note that any dust that is too cold to be observed with *Spitzer* would increase the dust-to-gas mass ratio above our inferred value.

Our current determination of the dust-to-gas mass ratio is quite uncertain, as we do not know the grain size distribution in the pre-shock gas. It is possible that models with a larger dust-to-gas ratio and a larger overabundance of small grains can be as viable as our current model with $R_V = 2.0$. This model degeneracy might be broken by future joint IR, X-ray, and UV studies focused on accurate determination of abundances of refractory elements in the postshock gas.

## 6. Summary

*Spitzer* observations of the entire region surrounding the remnant of SN 1006 show a clear detection of the NW filament at 24 $\mu$m, the same filament that is prominent in H$\alpha$ emission. IRS spectroscopy of this filament shows that the IR is produced entirely by continuum emission from warm dust grains, with a spectrum peaking somewhere beyond 35 $\mu$m. The

filament is not detected at 70 $\mu$m, likely due to the significantly higher background IR emission. The IR emission from the NW filament reaches its peak just inside of the H$\alpha$ emission, while the X-ray emission peaks still a little further behind. This is as expected, since H$\alpha$ emission should trace the exact location of the forward shock, while dust grains require a short amount of time to be heated to temperatures observable by *Spitzer* and then are sputtered away, while the post-shock gas requires even longer to become ionized enough to emit strongly at *Chandra* energies.

Fits to the *Spitzer* IRS spectrum taken at two positions along the NW filament, using models of collisionally-heated dust grains, do not tightly constrain the post-shock density $n_p$. The nominal best fit gives $n_p = 1.4 \pm 0.5$ cm$^{-3}$ (90%-confidence); we have adopted a model with $n_p = 1$ cm$^{-3}$, the value suggested from observations in other bands, for our subsequent analysis. The decay of the IR spatial profile behind the shock is far more rapid than expected from standard dust models. This is may be due in part to a high proportion of small dust grains in the ambient ISM at the location of SN 1006, high above the Galactic plane, and probably also results in part as a relic of the shock's having encountered a higher density region to the NW relatively recently. Nevertheless, it appears that sputtering rates significantly higher than those predicted by standard models will be required to fully explain the rapid decline in IR emission behind the shock.

Calculations of the dust-to-gas mass ratio in the ambient ISM indicate a value of approximately $1.5 \times 10^{-3}$, compared to the expected value of 5 $\times 10^{-3}$ for the Galaxy at the latitude of SN 1006. This difference of a factor of several is a phenomenon seen in virtually all IR/X-ray analyses of SNRs. The remnant of SN 1006 provides a rare opportunity to study the ISM high above the Galactic plane, and further IR, X-ray, and UV studies are necessary to understand this remnant.

This research is based on observations made with the *Spitzer* Space Telescope, which is operated by the Jet Propulsion Laboratory, California Institute of Technology under a contract with NASA. We are grateful to the support staff at IPAC for their guidance with some of the subtleties of *Spitzer* data analysis. We also acknowledge thoughtful comments from the anonymous referee, which have prompted us to, we hope, clarify much of this paper. Primary financial support for this project has been provided by NASA through RSA 1330031. PFW acknowledges additional support from the NSF through grant AST-0908566, and KJB acknowledges additional support from NASA through grant NNX11AB14G.

## REFERENCES

Acero, F., Aharonian, F., Akhperjanian, A. G., et al., & HESS Collaboration 2010, A&A, 516, A62

Acero, F., Ballet, J., & Decourchelle, A. 2007, A&A, 475, 883

Arendt, R. G. 1989, ApJS, 70, 181

Arendt, R. G., Dwek, E., Blair, W. P., Ghavamian, P., Hwang, U., Long, K. S., Petre, R., Rho, J., & Winkler, P. F. 2010, ApJ, 725, 585

Arnaud, K. A. 1996, in Astronomical Society of the Pacific Conference Series, Vol. 101, Astronomical Data Analysis Software and Systems V, ed. G. H. Jacoby & J. Barnes, 17

Ben Bekhti, N., Winkel, B., Richter, P., Kerp, J., Klein, U., & Murphy, M. T. 2012, A&A, 542, A110

Blair, W. P., Ghavamian, P., Long, K. S., Williams, B. J., Borkowski, K. J., Reynolds, S. P., & Sankrit, R. 2007, ApJ, 662, 998

Borkowski, K. J., Williams, B. J., Reynolds, S. P., et al. 2006, ApJ, 642, L141

Braun, R. 1987, A&A, 171, 233

Cassam-Chenaï, G., Hughes, J. P., Reynoso, E. M., Badenes, C., & Moffett, D. 2008, ApJ, 680, 1180

Chevalier, R. A., Kirshner, R. P., & Raymond, J. C. 1980, ApJ, 235, 186

de Kool, M., Li, H., & McCray, R. 1998, ApJ, 503, 857

Douvion, T., Lagage, P. O., Cesarsky, C. J., & Dwek, E. 2001, A&A, 373, 281

Draine, B. T. 2003, ARA&A, 41, 241

Draine, B. T. & Lee, H. M. 1984, ApJ, 285, 89

Dwek, E. 1987, ApJ, 322, 812

Dwek, E., Foster, S. M., & Vancura, O. 1996, ApJ, 457, 244

Dwek, E. & Scalo, J. M. 1980, ApJ, 239, 193

Dyer, K. K., Cornwell, T. J., & Maddalena, R. J. 2009, AJ, 137, 2956

Gardner, F. F. & Milne, D. K. 1965, AJ, 70, 754

Ghavamian, P., Winkler, P. F., Raymond, J. C., & Long, K. S. 2002, ApJ, 572, 888

Goldstein, B. R. 1965, AJ, 70, 105

Gomez, H. L., Clark, C. J. R., Nozawa, T., et al. 2012a, MNRAS, 420, 3557

Gomez, H. L., Krause, O., Barlow, M. J., et al. 2012b, ApJ, 760, 96

Heng, K. 2010, Publications of the Astronomical Society of Australia, 27, 23

Heng, K., van Adelsberg, M., McCray, R., & Raymond, J. C. 2007, ApJ, 668, 275

Katsuda, S., Long, K. S., Petre, R., Reynolds, S. P., Williams, B. J., & Winkler, P. F., ApJ, in press, http://arxiv.org/abs/1211.6443

Kirshner, R., Winkler, P. F., & Chevalier, R. A. 1987, ApJ, 315, L135

Kotak, R., Meikle, W. P. S., Farrah, D., Gerardy, C. L., et al. 2009, ApJ, 704, 306

Koyama, K., Petre, R., Gotthelf, E. V., Hwang, U., Matsuura, M., Ozaki, M., & Holt, S. S. 1995, Nature, 378, 255

Laming, J. M., Raymond, J. C., McLaughlin, B. M., & Blair, W. P. 1996, ApJ, 472, 267

Larson, K. A. & Whittet, D. C. B. 2005, ApJ, 623, 897

Lee, H.-G., Koo, B.-C., Moon, D.-S., Sakon, I., Onaka, T., Jeong, W.-S., Kaneda, H., Nozawa, T., & Kozasa, T. 2009, ApJ, 706, 441

Long, K. S., Reynolds, S. P., Raymond, J. C., Winkler, P. F., Dyer, K. K., & Petre, R. 2003, ApJ, 586, 1162

Marsden, B. C. 1965, AJ, 70, 126

Matsuura, M., Dwek, E., Meixner, M., et al. 2011, Science, 333, 1258

Mazzei, P. & Barbaro, G. 2011, A&A, 527, A34

Meikle, W. P. S., Kotak, R., Farrah, D., et al. 2011, ApJ, 732, 109

Miville-Deschênes, M.-A. & Lagache, G. 2005, ApJS, 157, 302

Nozawa, T., Kozasa, T., Tominaga, N., Maeda, K., Umeda, H., Nomoto, K., & Krause, O. 2010, ApJ, 713, 356

Nozawa, T., Maeda, K., Kozasa, T., Tanaka, M., Nomoto, K., & Umeda, H. 2011, ApJ, 736, 45

Planck Collaboration, Abergel, A., Ade, P. A. R., Aghanim, N., Arnaud, M., Ashdown, M., Aumont, J., Baccigalupi, C., Balbi, A., Banday, A. J., & et al. 2011, A&A, 536, A24

Putman, M. E., Peek, J. E. G., & Joung, M. R. 2012, ARA&A, 50, 491

Raymond, J. C., Korreck, K. E., Sedlacek, Q. C., Blair, W. P., Ghavamian, P., & Sankrit, R. 2007, ApJ, 659, 1257

Rho, J., Kozasa, T., Reach, W. T., Smith, J. D., Rudnick, L., DeLaney, T., Ennis, J. A., Gomez, H., & Tappe, A. 2008, ApJ, 673, 271

Rieke, G. H., Young, E. T., Engelbracht, C. W., et al. 2004, ApJS, 154, 25

Saken, J. M., Fesen, R. A., & Shull, J. M. 1992, ApJS, 81, 715

Sankrit, R., Williams, B. J., Borkowski, K. J., Gaetz, T. J., Raymond, J. C., Blair, W. P., Ghavamian, P., Long, K. S., & Reynolds, S. P. 2010, ApJ, 712, 1092

Schweizer, F. & Lasker, B. M. 1978, ApJ, 226, 167

Serra Díaz-Cano, L. & Jones, A. P. 2008, A&A, 492, 127

Smith, J. D. T., Armus, L., Dale, D. A., Roussel, H., Sheth, K., Buckalew, B. A., Jarrett, T. H., Helou, G., & Kennicutt, Jr., R. C. 2007, PASP, 119, 1133

Stephenson, F. R. 2010, Astronomy and Geophysics, 51, 050000

Stephenson, F. R. & Clark, D. H. 2002, Historical Supernovae and their Remnants (Oxford: Oxford U. Press), 150–174

Szalai, T., Vinkó, J., Balog, Z., Gáspár, A., Block, M., & Kiss, L. L. 2011, A&A, 527, A61

van den Bergh, S. 1976, ApJ, 208, L17

Vink, J., Laming, J. M., Gu, M. F., Rasmussen, A., & Kaastra, J. S. 2003, ApJ, 587, L31

Watson, D. 2011, A&A, 533, A16

Weingartner, J. C. & Draine, B. T. 2001, ApJ, 548, 296

Williams, B. J., Blair, W. P., Blondin, J. M., Borkowski, K. J., Ghavamian, P., Long, K. S., Raymond, J. C., Reynolds, S. P., Rho, J., & Winkler, P. F. 2011a, ApJ, 741, 96

Williams, B. J., Borkowski, K. J., Reynolds, S. P., Blair, W. P., Ghavamian, P., Hendrick, S. P., Long, K. S., Points, S., Raymond, J. C., Sankrit, R., Smith, R. C., & Winkler, P. F. 2006, ApJ, 652, L33

Williams, B. J., Borkowski, K. J., Reynolds, S. P., Ghavamian, P., Blair, W. P., Long, K. S., & Sankrit, R. 2012, ApJ, 755, 3

Williams, B. J., Borkowski, K. J., Reynolds, S. P., et al. 2011b, ApJ, 729, 65

Williams, B. J., Borkowski, K. J., Reynolds, S. P., et al. 2008, ApJ, 687, 1054

Winkler, P. F., Gupta, G., & Long, K. S. 2003, ApJ, 585, 324

Winkler, P. F. & Laird, F. N. 1976, ApJ, 204, L111

Wooden, D. H., Rank, D. M., Bregman, J. D., Witteborn, F. C., Tielens, A. G. G. M., Cohen, M., Pinto, P. A., & Axelrod, T. S. 1993, ApJS, 88, 477

Wright, E. L., Eisenhardt, P. R. M., Mainzer, A. K., et al. 2010, AJ, 140, 1868

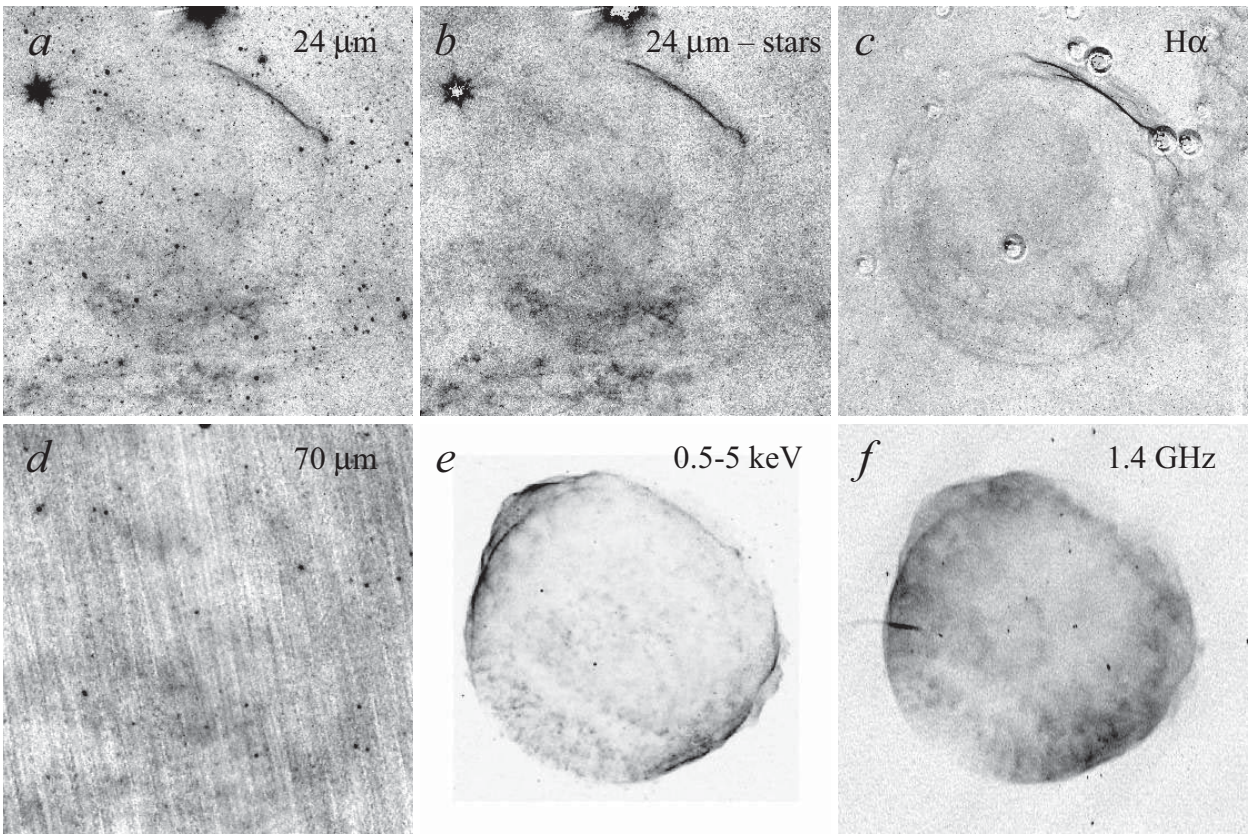


Fig. 1.— Images of SN 1006 in various bands. *Panel a:* Mosaic image at 24 $\mu$m, assembled from all four MIPS AORs. *b:* The same 24 $\mu$m mosaic, after subtraction of most point sources, displayed with a harder stretch. *c:* Deep H$\alpha$ image, after continuum subtraction to reveal the extremely faint shell of emission to the S and E (the NW filament is saturated in this display; the irregular donut-like patterns are artifacts, the residual images from bright stars—from Winkler et al. 2003). *d:* Mosaic image at 70 $\mu$m, from all four MIPS AORs. *e: Chandra* ACIS-I mosaic of SN 1006, from Cassam-Chenaï et al. (2008); this image emphasizes the synchrotron-dominated emission in the NE and SW. *f:* 1.4 GHz radio image, from Dyer et al. (2009). All the images are aligned, with a field 40′ square and oriented north up, east left.

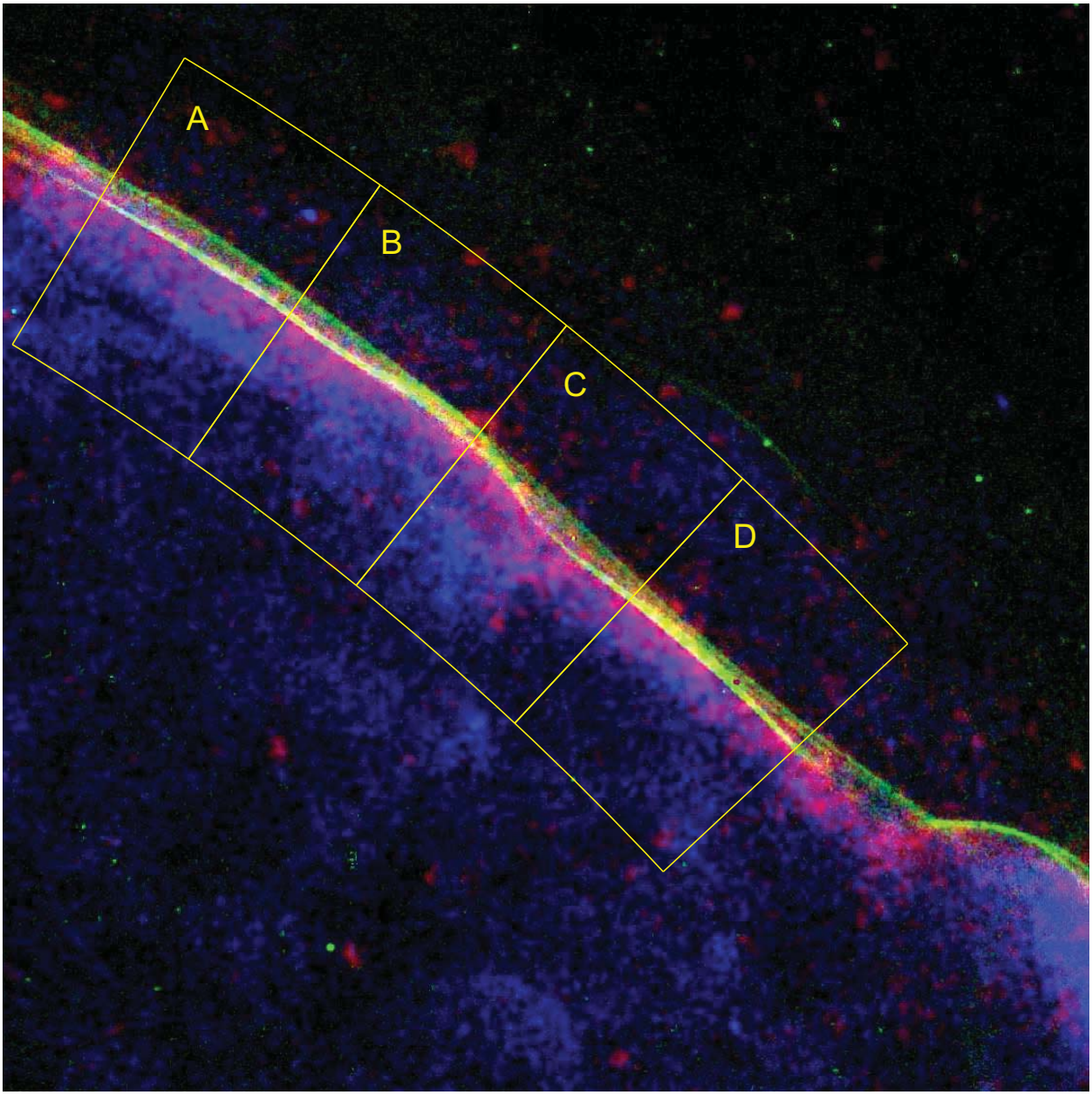


Fig. 2.— This 3-color image of the NW portion of SN 1006 shows the evolution in conditions behind the shock, which is propagating toward the NW (upper right corner). H$\alpha$ filaments (green, from Winkler et al. 2003) form immediately behind the shock; 24 $\mu$m emission (red) from warm dust trails slightly behind as the dust grains are first heated and then destroyed; X-rays (blue, 0.5 - 2.0 keV, from Long et al. 2003) peak further behind due to the ionization time to reach the species that are most effective at producing X-ray emission. The field is 6.5′ square; yellow regions indicate locations for the profiles shown in Fig. 3.

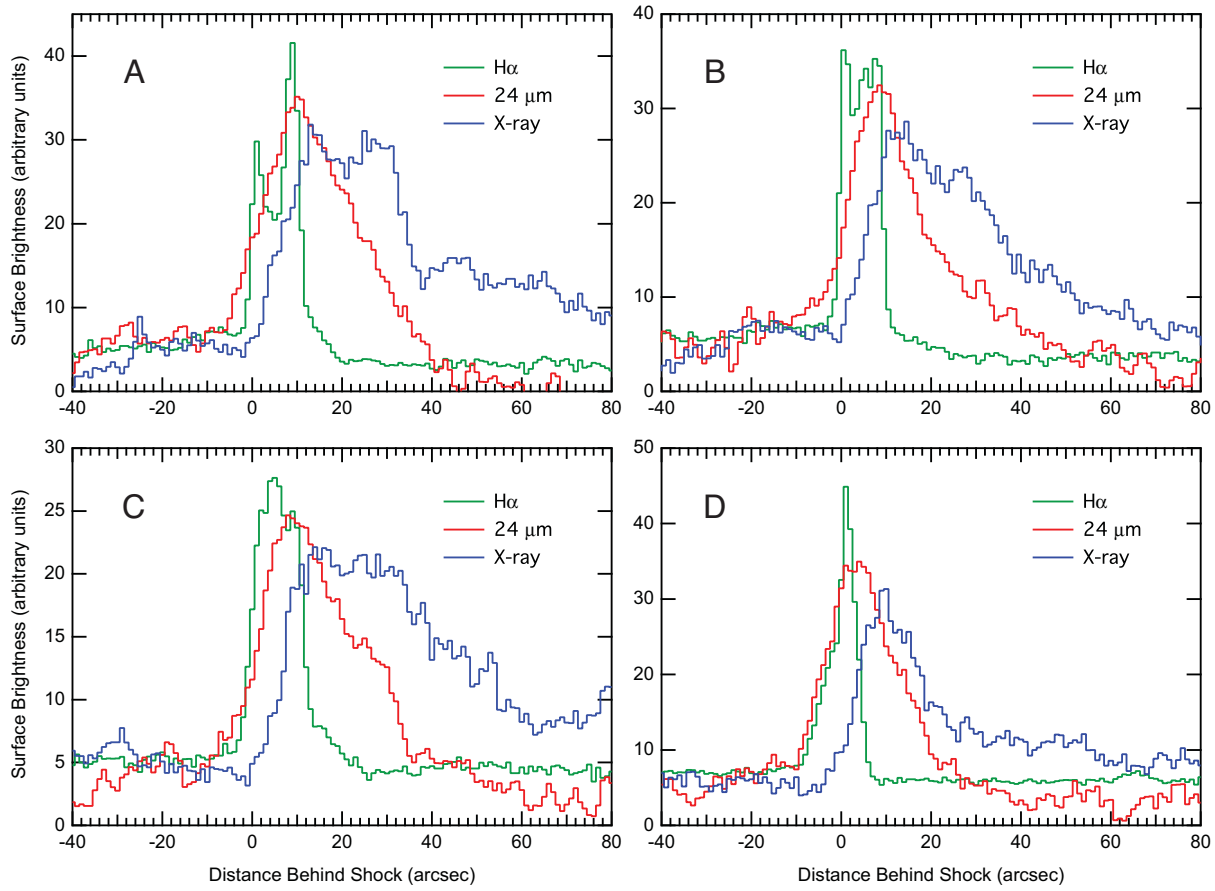


Fig. 3.— Radial profiles of emission in H$\alpha$, 24 $\mu$m, and X-rays, taken perpendicular to the shock, for the four regions shown in Figure 2. (The data sources are the same as for that figure.) In each case, the profiles run from outside the shell inward, and the shock location is arbitrarily taken as the point at which H$\alpha$ emission first rises sharply.

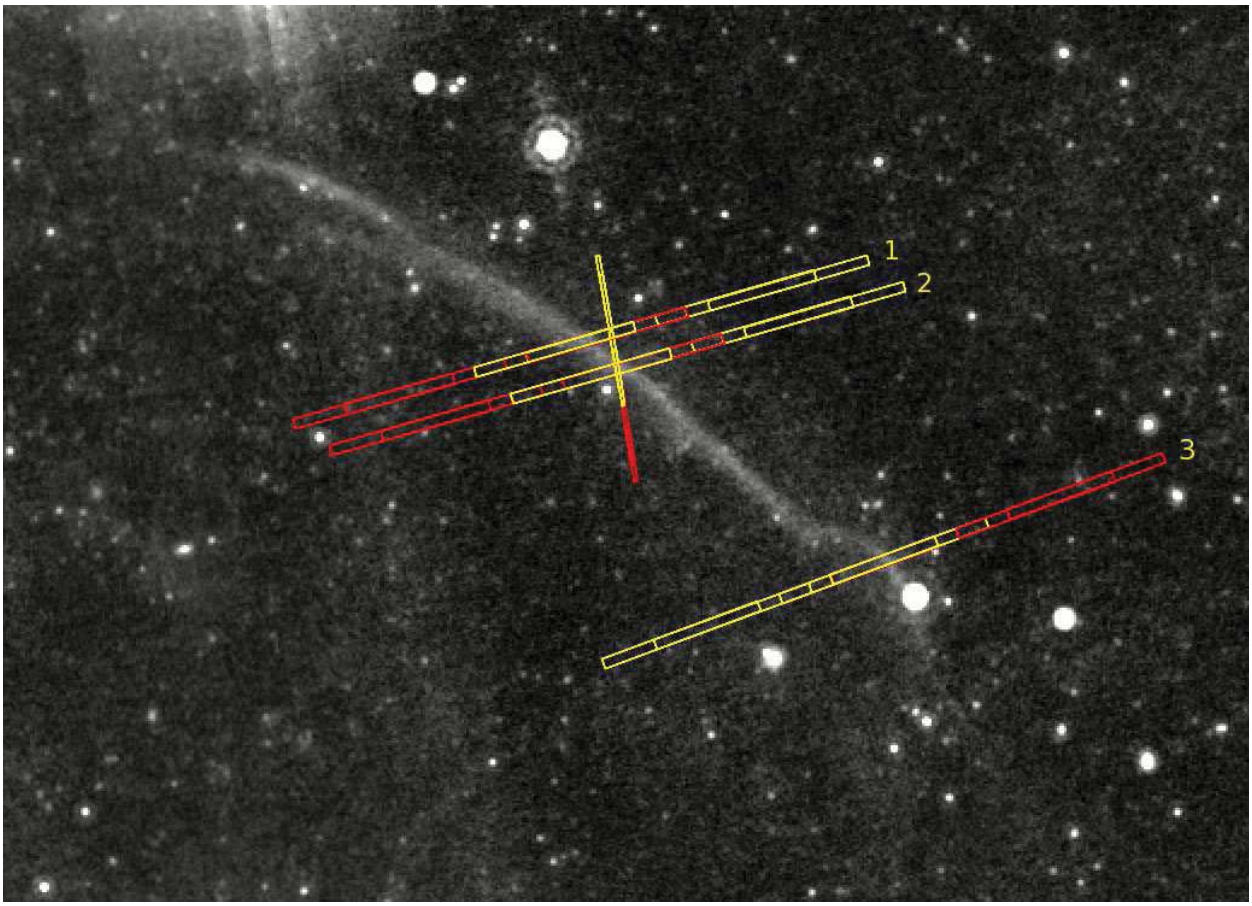


Fig. 4.— IRS positions superposed on the 24 $\mu$m image of the NW filament of SN 1006. Red rectangles correspond to the second order (longer wavelength) spectrographs, while yellow corresponds to first order. The three numbered slit positions are from long pointings with the IRS Long-Low instrument (14-40 $\mu$m). As we discuss in the text, we use positions 1 and 2 for our spectral modeling. The shorter, nearly vertical slit position is from the IRS Short-Low instrument, where no emission was detected.

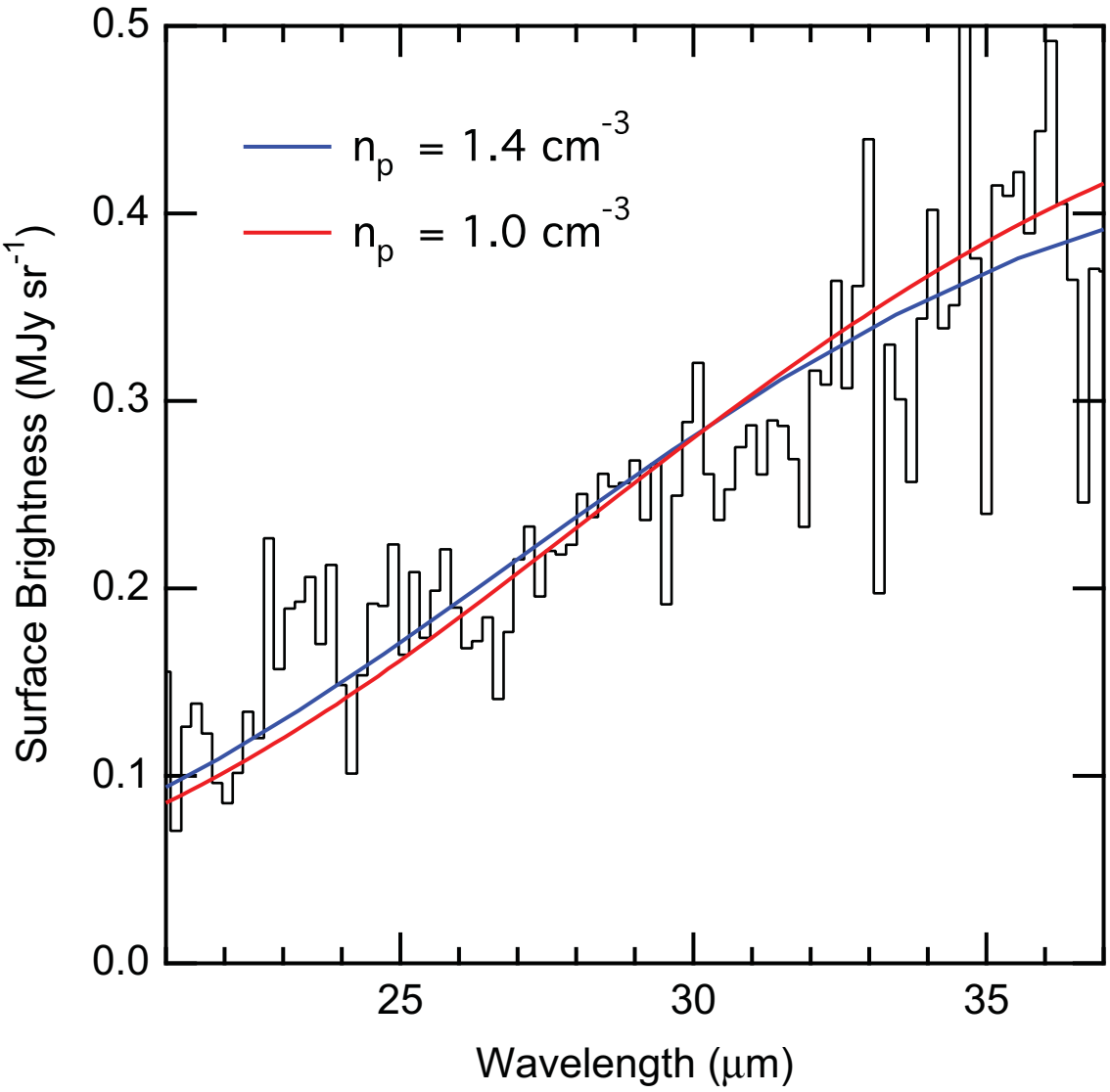


Fig. 5.— IRS spectrum, in black, combining positions 1 and 2 from Figure 4, and containing both orders of the Long-Low spectrograph. The points shown here, at wavelengths $> 21\mu$m, are all from order 1. The blue curve shows the nominal best-fit model, and gives a post-shock density in the filament of $n_p = 1.4$ cm$^{-3}$. The red curve shows a fit with the density constrained at $n_p = 1.0$ cm$^{-3}$, within the limits of acceptable fits, and consistent with observations in other bands (text, Section 5.1).

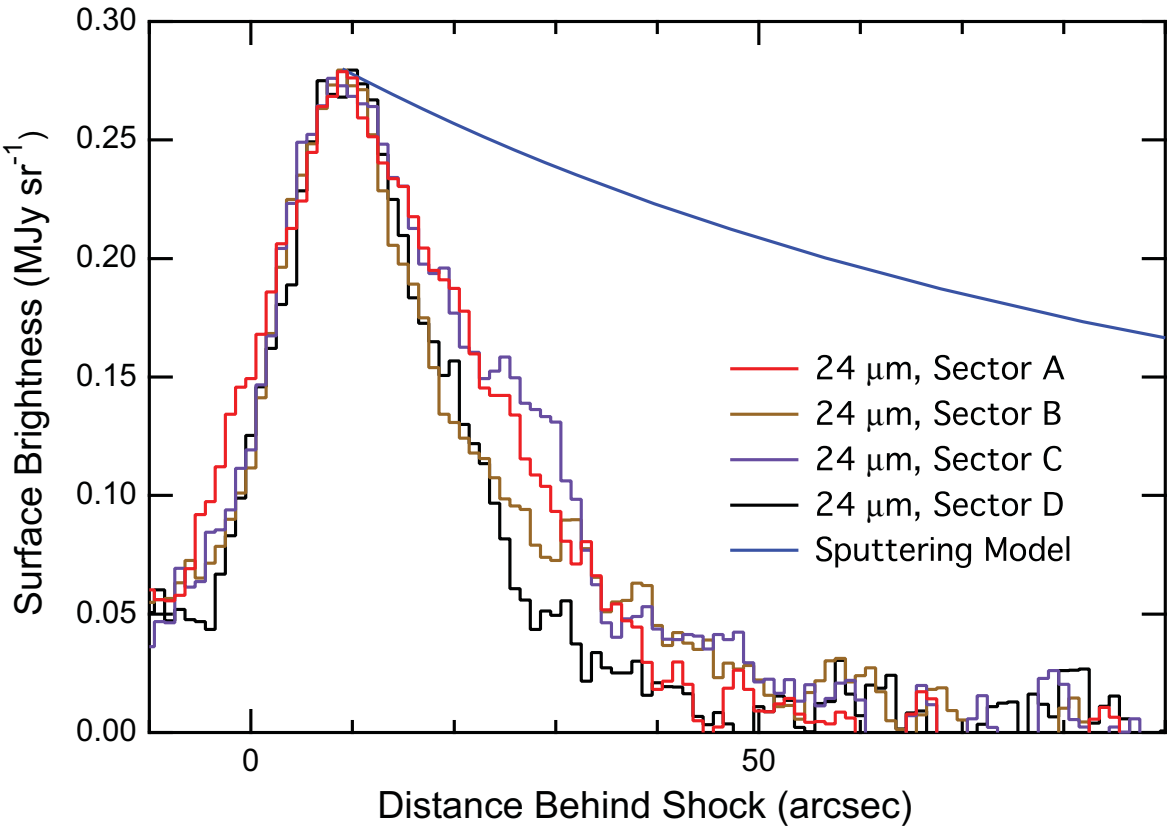


Fig. 6.— A comparison of radial profiles of the 24 $\mu$m emission (same as Fig. 3, scaled to a common peak intensity) with a model calculation, which has the post-shock proton density fixed at $n_p = 1\,\mathrm{cm}^{-3}$, consistent with observations in other bands (text, Section 5.1). A model assuming expansion into a uniform medium and normal sputtering rates decays far more slowly than the observations.